

pubs.acs.org/cm Article

# Structure and Stability of the Iodide Elpasolite, Cs<sub>2</sub>AgBil<sub>6</sub>

Kyle T. Kluherz, Sebastian T. Mergelsberg, James J. De Yoreo, and Daniel R. Gamelin\*



Cite This: Chem. Mater. 2023, 35, 5699-5708



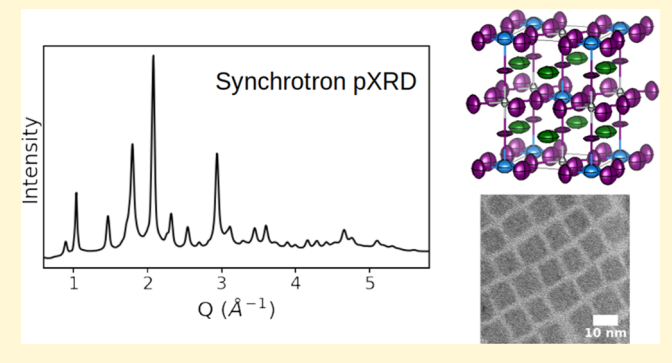
**ACCESS** 

III Metrics & More

Article Recommendations

SI Supporting Information

**ABSTRACT:** Iodide elpasolites (or double perovskites,  $A_2B'B''I_6$ ,  $B' = M^+$ ,  $B'' = M^{3+}$ ) are predicted to be promising alternatives to lead-based perovskite semiconductors for photovoltaic and optoelectronic applications, but no iodide elpasolite has ever been definitively prepared or structurally characterized. Iodide elpasolites are widely predicted to be unstable due to favorable decomposition to the competing  $A_3B_2I_9$  ( $B = M^{3+}$ ) phase. Here, we report the results of synchrotron X-ray diffraction (XRD) and X-ray total scattering measurements on putative  $Cs_2AgBiI_6$  nanocrystals made via anion exchange from parent  $Cs_2AgBiI_6$  nanocrystals. Rietveld refinement of XRD and pair distribution functions (PDF) data shows that these nanocrystals indeed exhibit a tetragonal  $(I\overline{4}m)$  elpasolite structure, making them the first



example of a structurally characterized iodide elpasolite. A series of experiments probing structural relaxation and the effects of surface ligation or grain size all point to the critical role of surface free energy in stabilizing the iodide elpasolite phase in these nanocrystals.

# INTRODUCTION

Lead-halide perovskites (APbX<sub>3</sub>) have been extensively studied due to their excellent optoelectronic properties and many potential applications, including photovoltaics, lighting, and Xray detection. 1-3 Recently, attention has turned to the possibility that elpasolites (or double perovskites, A2B'B"X6, where  $B' = M^+$ ,  $B'' = M^{3+}$ ) may serve as promising lead-free alternatives to the lead-halide perovskites. Although elpasolites generally do not exhibit the excellent emissive properties of certain lead-halide perovskites, some do show long carrier lifetimes and broad absorption, making them potentially suitable for applications in photovoltaics.<sup>4-7</sup> Some elpasolites also exhibit superior thermal and water stability compared to leadhalide perovskites, making them potentially attractive for devices that experience high temperatures under standard operation.<sup>8-11</sup> Numerous theoretical studies of elpasolites have predicted that iodide elpasolites, in particular, should exhibit the most suitable band gaps for photovoltaic applications. 5,12-18

Despite this broad interest and motivation, iodide elpasolites remarkably remain almost entirely unexplored experimentally. In fact, a recent review article <sup>12</sup> has highlighted that to date there have been *no* "structurally characterized" iodide elpasolites reported at all, asserting that their successful synthesis has so far been elusive. Computational models generally predict that iodide elpasolites are thermodynamically unstable relative to competing phases, explaining the paucity of experimental results. Although their enthalpies of formation may be favorable (*e.g.*,  $\Delta H_{\rm f} = -0.86$  eV/atom for 2CsI + BiI<sub>3</sub> + AgI  $\rightarrow$  Cs<sub>2</sub>AgBiI<sub>6</sub>), <sup>19</sup> they also appear to suffer from favorable

decomposition to the  $A_3B_2X_9$  (B =  $M^{3+}$ ) or  $A_3BX_6$  phases  $^{12,19}$  (e.g.,  $\Delta H_f = -0.41$  eV/atom for  $2Cs_2AgBiI_6 \rightarrow Cs_3Bi_2I_9 + 2AgI + CsI$ ). The X-ray diffraction (XRD) patterns of these primary competing phases can appear very similar to those of the elpasolites, complicating experimental analysis.  $^{9,20,21}$  We note that the thermodynamic properties of elpasolite nanocrystals (NCs) likely differ significantly from those estimated for bulk, but to our knowledge, no theoretical investigations have yet examined the stabilities of nanoscale elpasolites.

Nevertheless, syntheses of a few iodide elpasolites have been claimed, suggesting that it may indeed be possible to stabilize this family of materials under specific circumstances.  $Cs_2NaLaI_6$  was reported by Glodo et al.  $^{22}$  in 2006 and by Gundiah et al.  $^{23}$  in 2014, but the lack of structural characterization leaves unclear whether the material was actually an elpasolite. Zhang et al. reported powder XRD (pXRD) data for  $Cs_2NaBiI_6$  in 2018,  $^{24}$  along with Zheng et al. in 2022,  $^{25}$  but in both cases, the clear presence of a  $Cs_3Bi_2I_9$  contaminant and the strongly overlapping peaks of the two phases made definitive structural identification uncertain.  $Rb_2AgBiI_6$  was reported by Bhorde et al. in 2021,  $^{26}$  but with poor agreement between the experimental pXRD and the diffraction pattern calculated from a DFT model. Shadabroo

Received: June 16, 2023 Published: July 12, 2023





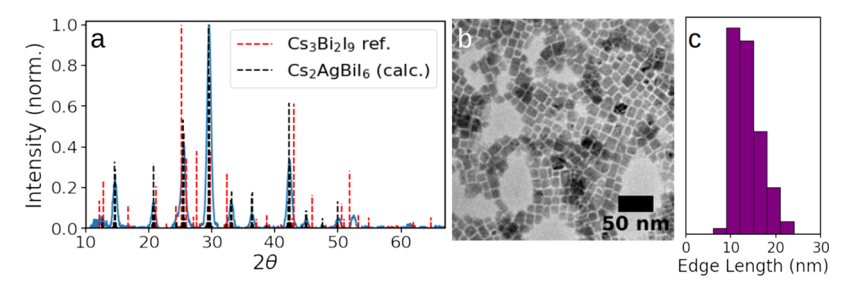


Figure 1. (a) Powder XRD data collected for  $Cs_2AgBiI_6$  nanocrystals prepared by anion exchange from  $Cs_2AgBiBr_6$  nanocrystals. A calculated pattern based on a hypothesized cubic  $(Fm\overline{3}m)$   $Cs_2AgBiI_6$  unit cell was used for initial identification.  $Cs_3Bi_2I_9$  was selected for comparison as the most similar known competing phase. (b) TEM image of  $Cs_2AgBiI_6$  nanocrystals. (c) Histogram of  $Cs_2AgBiI_6$  nanocrystal sizes measured from TEM images of  $\sim$ 200 nanocrystals.

et al.27 reported the formation of MA2AgBiI6 in 2021, and Cs<sub>2</sub>AgBiI<sub>6</sub> nanocrystals were reported by our group<sup>9</sup> and by Yang et al. 28 in 2018, but these materials were only structurally characterized with pXRD data that was insufficient to unambiguously identify them as iodide elpasolites. Notably, the absorption spectrum of Cs2AgBiI6 reported in ref 28 is different from that reported in ref 9 but is indistinguishable from that of one polymorph of Cs<sub>3</sub>Bi<sub>2</sub>I<sub>9</sub> (ref 20, vide infra). As a cautionary note, a thorough structural study of another potential iodide elpasolite, Cu<sub>2</sub>AgBiI<sub>6</sub>, using 100 K single-crystal XRD measurements found this material to exhibit a nonelpasolite trigonal R3m structure with layers of two-dimensional (2D) edge-sharing octahedra alternating with vacant octahedral sites. 21,29 The authors proposed that this alternating layer structure provides stability over the elpasolite structure in this case. Overall, there is thus little to no unambiguous evidence for the existence of any bone fide iodide elpasolites, making this family a remarkable void in the composition space of this important class of materials.

Here, we follow up on our previous claim<sup>9</sup> of Cs<sub>2</sub>AgBiI<sub>6</sub> elpasolite nanocrystals by reporting rigorous structural characterization of these nanocrystals via Rietveld refinement of synchrotron high-energy XRD (heXRD) data, analyzed in tandem with X-ray total scattering data. The data and analysis presented here yield the first unambiguous structure model of an iodide elpasolite, showing these nanocrystals to adopt the tetragonal I4m structure. We further demonstrate the critical role of nanostructuring, and especially of surface ligation, in stabilizing this phase and preventing decomposition to the competing Cs<sub>3</sub>Bi<sub>2</sub>I<sub>9</sub> product. These results firmly establish the existence of iodide elpasolites, a family of materials predicted to excel in optoelectronics applications but never previously available for experimental investigation. More broadly, these results highlight the power of chemistries unique to the nanoscale for accessing unprecedented compositions of matter.

## EXPERIMENTAL SECTION

**Materials.** Bi(OAc)<sub>3</sub>, Ag(OAc), Cs(OAc), trimethylsilyl iodide (TMSI), trimethylsilyl bromide (TMSBr), octadecene (90%), oleic acid (OA) (90%), oleylamine (OLA) (70%), 3-(N,N-dimethyloctadecylammonio)-propanesulfonate (sulfobetaine, >99%), benzyl alcohol (anhydrous, 99.8%), didodecyl-dimethylammonium bromide (DDDMABr), and trioctylphosphine (TOP, anhydrous, 90%) were purchased from Sigma-Aldrich and used without further purification. Hydrated reagents (OA, OLA, sulfobetaine, DDDMABr) were dried under vacuum for 4 h and then transferred into a glovebox before use in small-molecule addition experiments.

**Synthesis and Anion Exchange.** Cs<sub>2</sub>AgBiBr<sub>6</sub> nanocrystals (NCs) were synthesized using the procedure we reported previously (see ref 9 for details). Cs<sub>2</sub>AgBiI<sub>6</sub> NCs were made from these Cs<sub>2</sub>AgBiBr<sub>6</sub> NCs via

anion exchange using TMSI. 9,30 In a standard complete anion-exchange reaction, 1 mL of neat TMSI was added to 5 mL of a  $\sim$ 10  $\mu$ M Cs<sub>2</sub>AgBiBr<sub>6</sub> NC solution in hexanes, and the reaction vial was sealed for 1 day. The solution changed color from yellow to dark brown-red within  $\sim$ 10 s, but was allowed to sit to ensure complete anion exchange. Absorption, XRD, and energy-dispersive X-ray (EDX) data were collected to monitor the reaction progress. Thin-film samples of Cs<sub>2</sub>AgBiBr<sub>6</sub> were prepared by thermal evaporation as described previously.<sup>31</sup> Films were initially characterized in ambient atmosphere. For anion-exchange reactions, films were exposed to aliquots of TMSI vapor in a sealed glass vessel under inert atmosphere. For sequential TMSI exposures, the vessel's atmosphere was flushed with nitrogen between exposures. For thin-film heating experiments, samples (on Si and glass substrates) were heated directly on a temperature-controlled hot plate in a nitrogen glovebox. For NC heating experiments, colloidal samples were heated in a sealed glass vessel to minimize hexane evaporation.

**Small-Molecule Additions.** Small-molecule additions were performed in the following way: 5, 10, 20, or 100  $\mu$ mol of the selected compound (OA, OLA, benzyl alcohol, sulfobetaine, DDDMABr, and TOP) was added to 0.5 mL of 10  $\mu$ M Cs<sub>2</sub>AgBiX<sub>6</sub> (X = Br, I) NC solutions in hexanes, briefly stirred, then allowed to react overnight (~20 h). With the exception of sulfobetaine, which was added as a solid powder, 0.1 M solutions of each compound in hexanes were used for these reactions. We primarily report the results of the 20  $\mu$ mol additions. After additions, Cs<sub>2</sub>AgBiBr<sub>6</sub> samples were characterized using UV—vis absorption, XRD, and transmission electron microscopy (TEM), then exposed to 100  $\mu$ L of TMSI for anion exchange.

Sample Characterization. Absorption spectra were collected using an Agilent Cary 60. Benchtop powder XRD data were measured using a Bruker D8 Discover with a high-efficiency IµS microfocus X-ray source for Cu K $\alpha$  radiation operating at 50,000 mW (50 kV, 1 mA). NC samples were prepared by drop-casting NC stock solutions on silicon substrates. Samples were measured under Kapton film to prevent air exposure during measurement. TEM images were acquired using an FEI Tecnai G2 F20 supertwin microscope operating at 200 kV. A C2 aperture of 70  $\mu$ m was used to minimize beam damage. TEM EDX measurements were acquired using an EDAX-Elite-T detector. TEM measurements with in situ heating were performed using an FEI Titan 80-300 Environmental Transmission Electron Microscope (ETEM) with image correction. A Gatan double-tilt, furnace-based heating holder (model 646) was used for sample heating. Samples were first imaged, then heated to 100 or 120 °C for 10–30 min, then cooled to 30 °C before further imaging to avoid beam damage. NC stock solutions (10  $\mu$ M) were diluted by about one-fifth, and 5  $\mu$ L of the solution was deposited onto ultrathin carbon type A 400 Cu grids from TED Pella, Inc. Scanning electron microscopy (SEM) images were taken using an Apreos-S, and EDX mapping was performed at 10 kV, 800 pA, with a 100 ms dwell time.

**Pair Distribution Function (PDF) Measurements.** X-ray total scattering data were collected using beamline 11-ID-B at the Advanced Photon Source (APS) at Argonne National Laboratory.<sup>32</sup> Solutions of NC samples were measured at room temperature in quartz or Kapton capillaries using monochromatic X-rays with energy  $\sim$ 86.7 keV ( $\lambda$  =

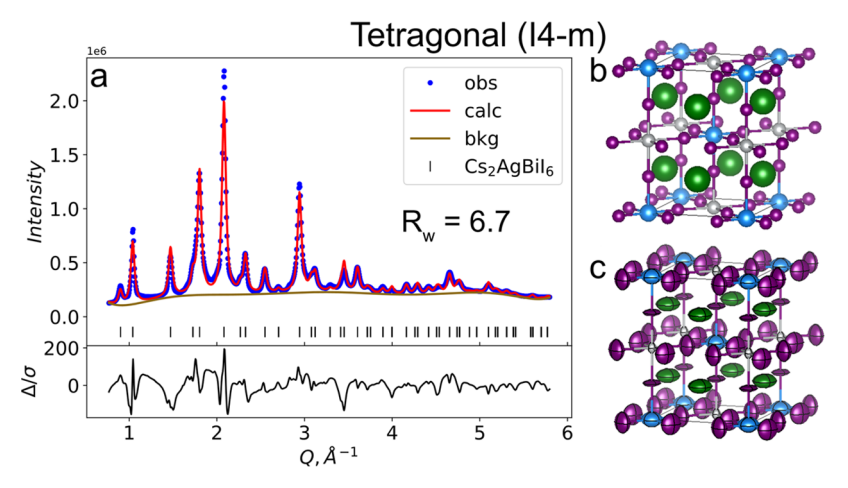


Figure 2. Rietveld refinement results using synchrotron X-ray scattering data for  $Cs_2AgBiI_6$  nanocrystals suspended in hexanes solution. (a) Data (blue dots), calculated pattern (red curve), background (brown curve), predicted peak positions (vertical black lines), and residual of fit  $(\Delta/\sigma)$  obtained using tetragonal  $\overline{I4m}$  structure. (b) Tetragonal  $\overline{I4m}$  structure model. Silver:  $Ag^+$ ; blue:  $Bi^{3+}$ ; green:  $Cs^+$ ; purple:  $I^-$ . (c) Structure model produced from (a), showing 95% atomic-displacement parameters refined using PDF data.

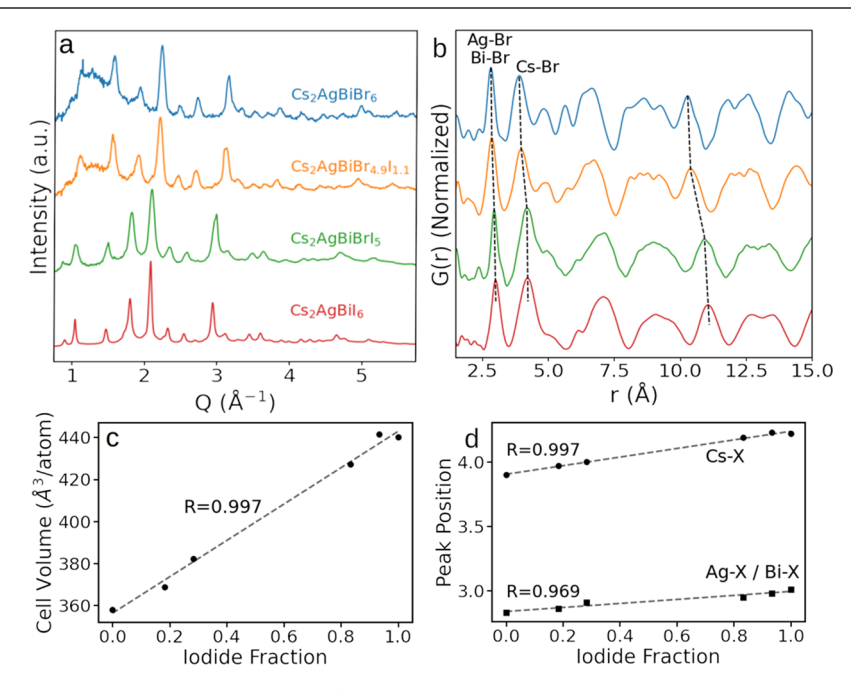


Figure 3. (a) High-energy XRD data for select  $Cs_2AgBi(Br_{1-x}I_x)_6$  nanocrystal samples from a stepwise anion-exchange reaction series, plotted in Q-space. The first two XRD curves show more noise and background because of weaker signals due to the use of less sample in the measurement. (b) Atomic pair distribution functions (PDFs, G(r)) for the same nanocrystal series, calculated from X-ray total scattering data. Specific peaks in the short-range order of  $Cs_2AgBiBr_6$  are labeled. Dashed lines trace peak positions across multiple samples for these two short-range order peaks as well as for one medium-range order peak. Fourier noise shows up as minor ripples in the PDF data. (c) Formula unit volumes obtained from Rietveld refinements of the full series of anion-exchanged samples, plotted as a function of fractional iodide content x in  $Cs_2AgBi(Br_{1-x}I_x)_6$ , where x is determined independently by EDX measurements. (d) Positions of the first two peaks (Ag-X/Bi-X and Cs-X) in the PDF data of panel (b), plotted as a function of fractional iodide content x. R values and linear best fits are shown for linear regressions to each peak.

0.1432 Å). Using a PerkinElmer 1621 a-Si area detector (200  $\mu \rm m^2$  pixel size), the sample-to-detector distance and detector nonorthogonality were calibrated with a CeO $_2$  standard (NIST 674a) diluted with glassy carbon. X-ray total scattering data were integrated using the GSAS-II software  $^{33}$  and a radial bin size of 1396, 1200, or 1000 for sample-to-detector distances of 250, 1000, and 1500 mm, respectively. Background subtraction and PDF processing were performed using the PDFgetX3 software.  $^{34}$  For PDF processing, a  $Q_{\rm max}$  of 28 Å $^{-1}$  and an  $r_{\rm max}$  of 30 Å were used. The PDFgui package  $^{35}$  was used to determine the instrument parameters of  $q_{\rm damp}=0.025$  and  $q_{\rm broad}=0.047$ , and to run r-space refinements to the PDF data. Rietveld refinements were calculated using the GSAS-II software,  $^{33}$  with an analytic Hessian algorithm run for three cycles for each refinement. Unit cell,

background (chebyschev-1 function, 9–15 terms), atom positions, and thermal parameters were refined. Fourier transforms of the backgrounds show no significant contribution of the elpasolite or secondary crystalline phases (Figure S4).

## RESULTS AND ANALYSIS

**Structural Characterization.** Figure 1 shows XRD and TEM data collected for Cs<sub>2</sub>AgBiI<sub>6</sub> NC samples prepared by the method we reported previously. As noted in ref 9, Cs<sub>2</sub>AgBiI<sub>6</sub> NCs will not form by direct hot-injection synthesis under our reaction conditions, and they are instead prepared *via* anion

exchange from parent  $Cs_2AgBiBr_6$  NCs that can be synthesized directly. The XRD data in Figure 1a are consistent with the predicted XRD pattern for the  $Cs_2AgBiI_6$  elpasolite phase (Figure S2), and notably show no identifiable peaks from the competing  $Cs_3Bi_2I_9$  phase. The TEM data in Figure 1b show cubic or near-cubic particles with an average edge length of ~14 nm (Figure 1c) measured across ~200 particles. Overall, these data are essentially indistinguishable from the results we reported previously, demonstrating the reproducibility of the synthesis methods from Creutz et al., and indicating that the findings of this study are applicable to the materials reported in that previous study.

Although compelling, the XRD data in Figure 1a are insufficient to unambiguously determine the structure of these Cs<sub>2</sub>AgBiI<sub>6</sub> NCs. In particular, the data do not allow distinction among the three variants of elpasolites, the trigonal  $(R\overline{3}m)$ , cubic (Fm3m), and tetragonal  $(\overline{I4m})$  structures. More powerful structural data were therefore obtained. Figure 2 shows highenergy X-ray scattering data collected for the same Cs<sub>2</sub>AgBiI<sub>6</sub> NCs using a synchrotron source at the APS. Using these data, we calculated Rietveld refinement structure fits to the cubic, tetragonal, and trigonal elpasolite structures using GSAS-II.<sup>33</sup> The trigonal structural model yielded a poor fit with an overall weighted R factor  $(R_w)$  of 13.7 (see Figure S6) and was not considered further. The cubic  $Fm\overline{3}m$  structural model gave a better fit, with an  $R_{\rm w}$  of 7.8 and low residual values (see Figure S3), but inspection of the computed structure revealed unusually large thermal disorder within the Ag+ sublattice (Figure S3c). Fixing these thermal parameters to the literature values found for Ag<sup>+</sup> in Cs<sub>2</sub>AgBiBr<sub>6</sub> (ICSD# 239875), which is known to be cubic  $(Fm\overline{3}m)$ , 36 yielded a substantially poorer fit (Figure S5), with  $R_w = 12.9$ , and generated notable new residual peaks around 1.8 and 3.1 Å<sup>-1</sup>. Close inspection found these large residuals to correlate with low-symmetry splittings of the (3,1,1) and (5,3,1) peaks, confirming a lower-symmetry structure. Rietveld refinement using a tetragonal I4m structure (Figure 2a,b) yielded a much improved fit  $(R_w = 6.7)$  to the data. Notably, the lower  $R_{\rm w}$  relative to the  $Fm\overline{3}m$  fit is also accompanied by thermal parameters (Figure 2c) very similar to those found in other elpasolite structures in the ICSD (Coll. Codes 239875, 11523, 18989, 21475, 32193). We therefore conclude that our Cs<sub>2</sub>AgBiI<sub>6</sub> NCs are best described by a tetragonal I4m elpasolite structure. This structure (Figure 2b) is characterized by lattice parameters of a = b = 8.535(4) Å and c =12.080(4) Å, a unit cell volume of 880 Å<sup>3</sup>, and a distorted Bi-I octahedron with Bi-I bond distances of 2.91 (4 bonds) and 3.03 Å (2 bonds). The full structural details are cataloged in the accompanying cif file (see SI) and have been deposited in the Inorganic Crystal Structure Database hosted by the Cambridge Crystallographic Data Centre (CCDC). To our knowledge, these results represent the first complete structural characterization of any iodide elpasolite.

To supplement the above analysis of the Cs<sub>2</sub>AgBiI<sub>6</sub> structure, we additionally investigated the structure's evolution during the conversion of the NCs from cubic Cs<sub>2</sub>AgBiBr<sub>6</sub> to tetragonal Cs<sub>2</sub>AgBiI<sub>6</sub> by anion exchange. Figure 3 presents the heXRD and pair distribution functions (PDF) from X-ray total scattering data collected for a series of intermediate anion-exchange reactions. Dashed lines in Figure 3b trace the progression of select peak positions across the sample series for ease of viewing. The first two peaks correspond to specific atom pairs and both show gradual shifts to larger *r*. The third is included to demonstrate that the same shift occurs in the medium-range

order. Figure 3c,d summarizes these data by plotting formula unit volume  $(V_f)$  and PDF peak positions vs the fractional iodide content x in  $Cs_2AgBi(Br_{1-x}I_x)_6$  measured by EDX. These data all increase linearly with x, reflecting lattice accommodation of the larger iodide anions. Both the heXRD and the PDF (Figure 3a,b) data thus reveal continuous shifts in feature positions across the entire sample set, with no abrupt or discontinuous transitions between the two end points. PDF is especially useful in the analysis of this conversion due to its high sensitivity to the presence of minority phases, which appear as new peaks or shoulders in G(r) regardless of crystallinity. <sup>37–39</sup> Notably, the data in Figure 3b show no new peaks emerging during anion exchange, again supporting a gradual structural evolution with anion exchange. The data in Figure 3 thus show no evidence of mixed-phase or exsolved-phase compositions at any of the intermediate stages of anion exchange, and we conclude that these materials transition continuously from the cubic Cs<sub>2</sub>AgBiBr<sub>6</sub> structure to the tetragonal Cs<sub>2</sub>AgBiI<sub>6</sub> structure via incremental lattice expansion during anion exchange. This conclusion is similar to that drawn for lead-halide perovskite NCs (CsPbX<sub>3</sub>), which also convert from chloride to bromide to iodide compositions with no detectable intermediate or exsolved phases. 30,40-42 Importantly, the gradual evolution of these data in conjunction with the fact that Cs<sub>2</sub>AgBiBr<sub>6</sub> is a wellestablished elpasolite structure bolsters our conclusion that Cs<sub>2</sub>AgBiI<sub>6</sub> retains an elpasolite structure as well.

Stability of the lodide Elpasolite Structure. After establishing that these iodide NCs form the tetragonal I4m elpasolite structure, we turn to the question of phase stability, in view of the absence of any other structurally characterized iodide elpasolites and the theoretical predictions that these structures should spontaneously decompose into more stable phases. 5,7,11,13 We may consider two general hypotheses: (1) this iodide elpasolite structure is kinetically trapped, perhaps as a result of anion exchange from a parent bromide elpasolite, and (2) this iodide elpasolite structure is thermodynamically stable, but only because of its surface free energy when prepared at the nanoscale. On the one hand, our unsuccessful attempts to prepare Cs<sub>2</sub>AgBiI<sub>6</sub> NCs directly via hot-injection synthesis using TMSI<sup>9</sup> that leave anion exchange from the corresponding bromide NCs as the only synthesis route could suggest that the Cs<sub>2</sub>AgBiI<sub>6</sub> composition is kinetically trapped. On the other hand, it is difficult to reconcile the notion of a kinetic barrier to ion reorganization with the observation of high ion mobility in these materials during anion exchange. This consideration could suggest instead that the iodide elpasolite NCs are thermodynamically favorable but their direct synthesis is impeded by other kinetically competitive processes, mainly  $Cs_3Bi_2I_9$ formation.9

Stabilization of metastable polymorphs at the nanoscale is well known, <sup>43–45</sup> generally resulting from the increased importance of surface free energy, and Cs<sub>2</sub>AgBiI<sub>6</sub> may be a new example of this phenomenon. Investigating the possibility that surface energy stabilizes these Cs<sub>2</sub>AgBiI<sub>6</sub> NCs, we considered two potential sources: structural relaxation at or near the crystal surfaces, and reduction in interfacial free energy due to ligand adsorption. We therefore sought to test both of these hypotheses. To investigate the first, we performed fits to the PDF data for both the tetragonal and cubic structure models (see Figures S8 and S9, SI) and examined these for evidence of structural relaxation. These fits show the greatest differences in the short-range order, consistent with greater deviation from periodicity at the crystal surfaces (which contribute dispropor-

tionately to the short-range order for 14 nm NCs), hence suggesting lattice relaxation associated with the crystallite surfaces. These data thus suggest that surface relaxation may play an important role in stabilizing the elpasolite phase on the nanoscale, despite the expected thermodynamic instability of this phase in bulk.<sup>13</sup>

If reduction in interfacial free energy due to ligand adsorption enhances the stability of these iodide elpasolite NCs, then their stability might be expected to depend on the types and quantities of surface ligands present. Although prior work has specifically addressed the influence of various potential surface ligands on the degradation of CsAgMX<sub>6</sub> chloride and bromide elpasolite NCs (including Cs<sub>2</sub>AgBiBr<sub>6</sub>),  $^{46,47}$  such experiments on iodide elpasolite NCs have not been reported. In refs 46 and 47, excess primary and tertiary amines were found to be particularly potent for causing complete dissolution of the CsAgMX<sub>6</sub> (X = Cl, Br) NCs, attributed to Ag diffusion and the formation of Cs<sub>3</sub>Bi<sub>2</sub>Br<sub>9</sub> and Cs<sub>3</sub>BiBr<sub>6</sub> phases,  $^{46}$  or to  $M^{3+}$  extraction and formation of Cs<sub>2</sub>AgCl<sub>3</sub>.

To investigate the influence of surface ligation on the stability of the iodide elpasolite NCs described here, we performed a series of small-molecule addition experiments in conjunction with the anion-exchange reactions described above, monitored by a combination of XRD, absorption spectroscopy, and TEM. For reference, Figure 4 highlights key contrasts between the absorption spectra and XRD patterns of Cs<sub>2</sub>AgBiI<sub>6</sub> and its primary decomposition product, Cs<sub>3</sub>Bi<sub>2</sub>I<sub>9</sub>. The Cs<sub>2</sub>AgBiI<sub>6</sub> absorption spectrum is characterized by a broad onset with shoulders at 390 and 530 nm, whereas Cs<sub>3</sub>Bi<sub>2</sub>I<sub>9</sub> shows more pronounced peaks at 356 and 481 nm along with a shoulder around 420 nm. As noted previously, Cs<sub>2</sub>AgBiI<sub>6</sub> and Cs<sub>3</sub>Bi<sub>2</sub>I<sub>9</sub>

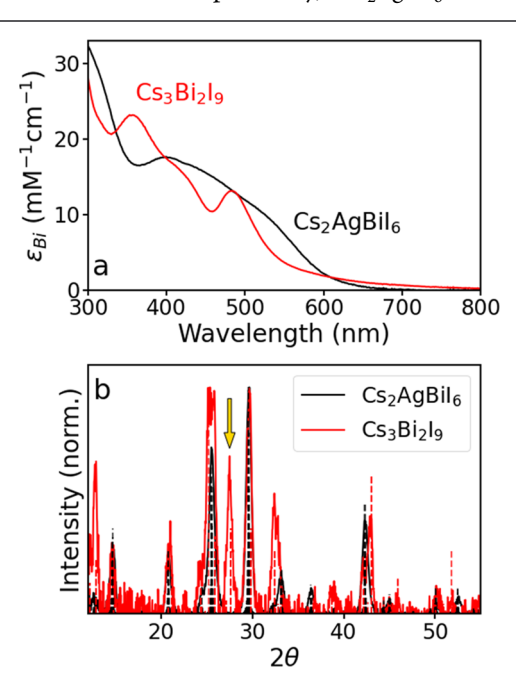


**Figure 4.** Comparison of (a) absorption spectra (with molar extinction coefficients referenced to  $\mathrm{Bi}^{3+}$ ) and (b) XRD patterns for  $\mathrm{Cs}_2\mathrm{AgBiI}_6$  and  $\mathrm{Cs}_3\mathrm{Bi}_2\mathrm{I}_9$  nanocrystals, both made via hot injection. The absorption spectra show clear differences in peak positions and shapes between the two compositions. Note that there is some uncertainty in the precise extinction coefficients due to potential error from the determination of the  $\mathrm{Bi}^{3+}$  concentrations. The arrow in (b) highlights a major reflection present in  $\mathrm{Cs}_3\mathrm{Bi}_2\mathrm{I}_9$  that is lacking in  $\mathrm{Cs}_2\mathrm{AgBiI}_6$ . These contrasts can be used to distinguish between these two phases.

XRD patterns are very similar, due to their similar unit cells, but a signature peak at  $27.5^{\circ}$  can be used to identify the presence of  $Cs_3Bi_2I_9$ . Such contrasts help to distinguish between these two compounds and to track any NC decomposition.

Figure 5 shows XRD data for representative anion exchange and small-molecule addition reactions, and additional data are

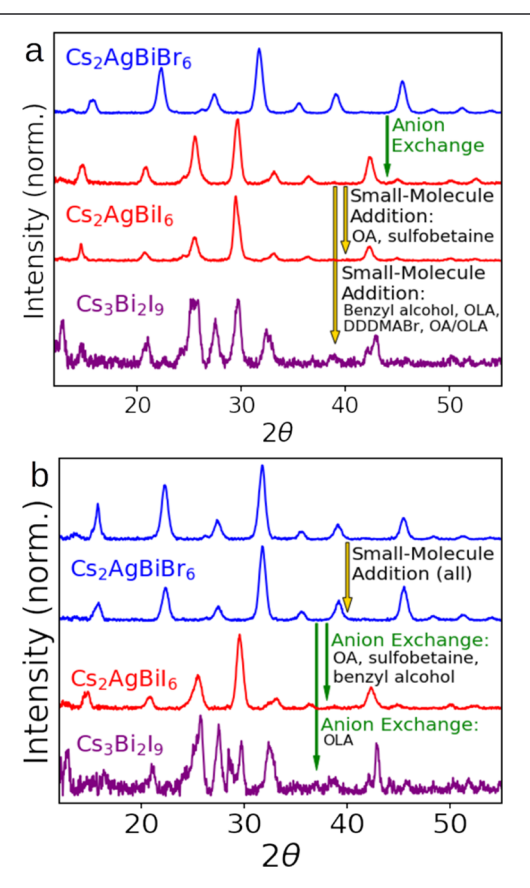


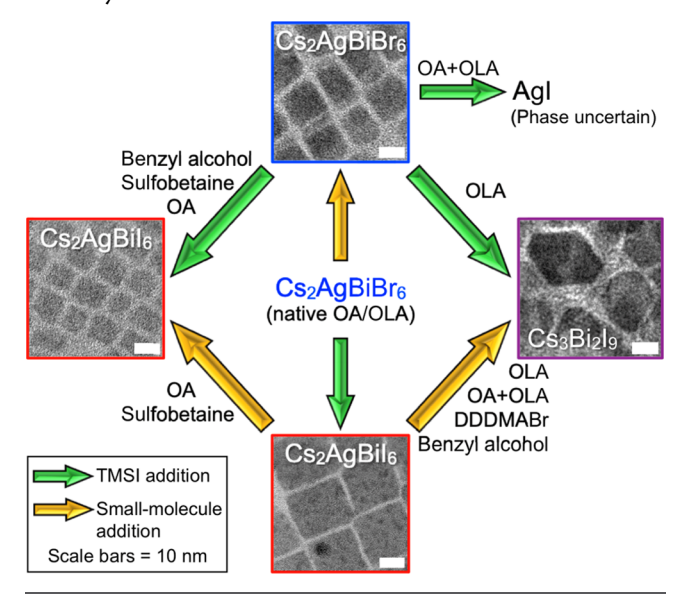
Figure 5. Representative XRD data describing the results of anion-exchange and small-molecule addition reactions involving  $Cs_2AgBiX_6$  (X = Br, I) nanocrystals. (a) Anion exchange followed by small-molecule addition. Addition of oleic acid (OA, data shown here) or sulfobetaine to  $Cs_2AgBiI_6$  nanocrystals retains the elpasolite structure, but the addition of oleylamine (OLA), 50:50 (mol) OA/OLA, benzyl alcohol (data shown here), or didodecyl-dimethylammonium bromide (DDDMABr) transforms the  $Cs_2AgBiI_6$  elpasolite nanocrystals into  $Cs_3Bi_2I_9$  nanocrystals. (b) Small-molecule additions followed by anion exchange.  $Cs_2AgBiBr_6$  nanocrystals retain the elpasolite structure following additions of all small molecules investigated here. Anion exchange for samples with added OA, sulfobetaine, or benzyl alcohol (data shown here) yields elpasolite  $Cs_2AgBiI_6$  nanocrystals. Anion exchange for samples with added OLA yields  $Cs_3Bi_2I_9$  nanocrystals.

provided in the SI. Figure 5a shows results from anion exchange using TMSI (*i.e.*,  $Cs_2AgBiBr_6 + TMSI \rightarrow Cs_2AgBiI_6 + TMSBr)^{9,30}$  followed by the addition to the NC solution of one of a set of small molecules that included OA, OLA, sulfobetaine, DDDMABr, and benzyl alcohol. Our NC synthesis was performed in the presence of a mixture of OA and OLA, and further additions of each of these native ligands were thus tested. Sulfobetaine was chosen as a zwitterionic ligand based on its effectiveness in binding to lead-halide perovskite NC surfaces. DDDMABr was selected as an example of a quaternary ammonium species that binds strongly to the surfaces of CsPbBr<sub>3</sub> NCs. Benzyl alcohol has been reported to influence ligand binding in perovskite NCs, and may remove surface

ligands. Each of these compounds was added to  $\sim 1 \mu M$  NC solutions at concentrations ranging from  $\sim 1$  to  $\sim 100 \mu M$ . For comparison, Figure 5b shows results from inverting the sequence of additions, i.e., small-molecule addition to a Cs<sub>2</sub>AgBiBr<sub>6</sub> NC solution, followed by anion exchange. From these data, we observe that the Cs<sub>2</sub>AgBiBr<sub>6</sub> NCs retain their elpasolite structure upon exposure to all of the compounds tested here, whereas the Cs<sub>2</sub>AgBiI<sub>6</sub> NCs are far more sensitive, retaining the elpasolite phase with OA or sulfobetaine but transforming to other phases for all other additives examined. The data for the Cs<sub>2</sub>AgBiBr<sub>6</sub> NCs did show small impurity peaks after exposure to OLA (Figure S14), but these NCs were substantially more stable than the Cs2AgBiI6 NCs against degradation by this ligand even at high OLA concentrations, and the dominant phase remained the elpasolite. Additionally, anion exchange in the presence of 50:50 (molar) OA/OLA yielded AgI as the primary product (with evidence of other unidentified minority phases), compared to Cs<sub>2</sub>AgBiI<sub>6</sub> when just OA was present. Further details of these results are provided in the Supporting Information (SI).

Scheme 1 summarizes the full set of results from these experiments graphically. The arrows denote the reactions that

Scheme 1. Summary of Anion-Exchange and Various Small-Molecule Addition Reactions of  $Cs_2AgBiX_6$  (X = Br, I) Nanocrystals



were performed and connect the starting and isolated product compositions for each reaction. The small-molecule additives present during each reaction are shown next to the various arrows. This scheme highlights the different susceptibilities of Cs<sub>2</sub>AgBiBr<sub>6</sub> and Cs<sub>2</sub>AgBiI<sub>6</sub> NCs to decomposition. Beginning with the parent Cs2AgBiBr6 NCs, neither anion exchange nor small-molecule addition causes substantial degradation. From the resulting NCs, however, further chemistry results in a multitude of degradation products. Although Cs<sub>2</sub>AgBiBr<sub>6</sub> retains its phase upon exposure to the additives examined here, only oleic acid and sulfobetaine preserve the elpasolite structure of Cs<sub>2</sub>AgBiI<sub>6</sub>. Note the pathway-dependent chemical transformations in the case of benzyl alcohol: its addition to Cs<sub>2</sub>AgBiBr<sub>6</sub> NCs followed by anion exchange yields Cs<sub>2</sub>AgBiI<sub>6</sub> NCs, whereas its addition to Cs<sub>2</sub>AgBiI<sub>6</sub> NCs after anion exchange yields a Cs<sub>3</sub>Bi<sub>2</sub>I<sub>9</sub> decomposition product. Additionally,

TEM shows the retention of NC size for all reactions, with a morphology change to hexagonal crystals for the hexagonal Cs<sub>3</sub>Bi<sub>2</sub>I<sub>9</sub> decomposition product. We note an apparent correlation between anionic ligands (oleate and sulfobetaine) and stabilities of Cs<sub>2</sub>AgBiI<sub>6</sub> NCs. It is conceivable that the anionic ligands stabilize the iodide elpasolite NCs by passivating surface anion vacancies. Alternatively, although elpasolite decomposition appears to retain the NC size, we cannot neglect the possibility that some of these additives actively drive decomposition through ion-selective microsolvation. Further investigation will be necessary to fully understand the surface chemistry of this new family of nanomaterials. Nonetheless, we conclude from these results that the stability of elpasolite Cs<sub>2</sub>AgBiI<sub>6</sub> NCs is indeed highly sensitive to their surface chemistry, and a high surface-to-volume ratio alone is not sufficient to stabilize the elpasolite phase.

In a separate line of interrogation, we then performed a series of experiments aimed at probing the dependence of Cs<sub>2</sub>AgBiI<sub>6</sub> stability on temperature and NC size. Thermal stability was probed by both ex situ and in situ measurements. For the ex situ experiments, Cs<sub>2</sub>AgBiI<sub>6</sub> NCs were deposited onto Si substrates and their structures were monitored as a function of anaerobic anneal temperature and time using XRD and SEM (Figures S18 and S19). The  $Cs_2AgBiI_6$  NCs were stable up to ~100 °C, above which they began to decompose into a mixture of Cs<sub>3</sub>Bi<sub>2</sub>I<sub>9</sub>, CsI, and AgI, with Cs<sub>3</sub>Bi<sub>2</sub>I<sub>9</sub> dominating the XRD patterns (Figure S18). Full decomposition was observed at 125 °C. Moreover, SEM of the Cs<sub>3</sub>Bi<sub>2</sub>I<sub>9</sub> product (Figure S19) revealed extensive particle sintering. Heating for 2 h at temperatures below 100 °C caused no decomposition. These results demonstrate that the decomposition of Cs<sub>2</sub>AgBiI<sub>6</sub> NCs is thermally activated. Very similar results are obtained from in situ XRD measurements during heating in air (Figure S20).

From the above observations, we hypothesized that decomposition may be linked to the reduced surface-to-volume ratios in the larger crystallites that form upon sintering, i.e., the reduced influence of surface free energy. To test this hypothesis, we prepared samples that deliberately contained broad size distributions. For example, Figure 6 shows XRD, TEM, and electron diffraction (ED) data for a sample containing a mixed population of nanocubes ( $L \sim 15$  nm) and nanorods ( $L \sim 200$ nm,  $W \sim 15$  nm). TEM shows that nanorods are the dominant species in this sample, but critically, XRD confirms the presence of only the elpasolite phase (Figure 6a), contrary to the above hypothesis. Electron diffraction (Figure 6c) from the area imaged in Figure 6b shows signature arcs (denoted with red arrows) corresponding to preferential diffraction from the onedimensional nanorods, associated with net spatial orientation of the nanorods in Figure 6b. These arcs overlay the elpasolite diffraction rings, confirming that these nanorods share the iodide elpasolite structure. There is thus no evidence for a correlation between particle size and phase transformation in this size regime.

We then hypothesized that decomposition may be associated with the combination of heat and particle size. To test this hypothesis, we performed *in situ* heating during TEM measurements of another sample possessing a deliberately broad size distribution (Figures S21 and S22). Again, we found no correlation between particle size and decomposition, nor did we generally observe particle sintering upon heating. Some particles transformed and sintered at 100 °C while others of the same size persisted as elpasolites even to 120 °C (Figure S21). Additionally, other NCs decomposed without changing size or

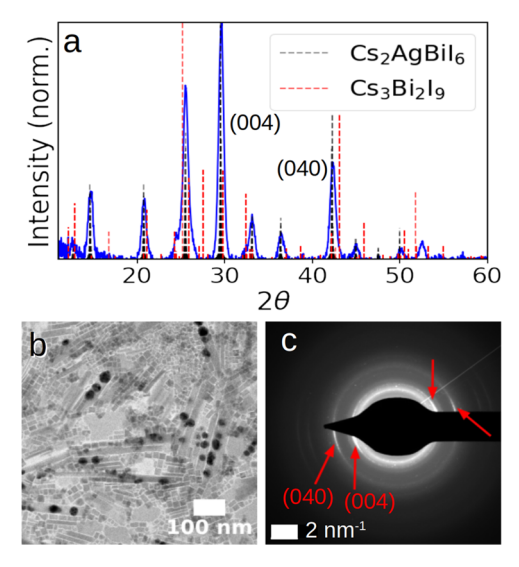


**Figure 6.** (a) XRD, (b) TEM, and (c) electron diffraction (ED) of a  $Cs_2AgBiI_6$  sample with a mixed population of nanocubes and one-dimensional (1D) nanorods. The red arrows in (c) identify diffraction arcs corresponding to the nanorods. Note the net spatial alignment of the rods in panel (b), giving rise to the arcs in panel (c).

sintering with their neighbors. We conclude that phase transformation and particle sintering are not linked and instead can occur independently upon heating. Instead, the results suggest that the critical factor in the thermally induced phase transformation of Cs<sub>2</sub>AgBiI<sub>6</sub> is likely the loss of surface ligands. In support of this conclusion, we have found that colloidal Cs<sub>2</sub>AgBiI<sub>6</sub> NCs retain the Cs<sub>2</sub>AgBiI<sub>6</sub> phase even when heated in solution to 140 °C (Figure S23), beyond the ~100-125 °C decomposition temperature of the same NCs on a solid substrate. Collectively, these results provide strong support for the conclusion that surface ligands are a primary factor determining the stability of the Cs<sub>2</sub>AgBiI<sub>6</sub> elpasolite phase and preventing its transformation to Cs<sub>3</sub>Bi<sub>2</sub>I<sub>9</sub>, and that reduced dimensionality is necessary but not sufficient. Given these findings, we hypothesize that judicious choice or exclusion of surface ligands, possibly in conjunction with other crystallite size and surface modifications (e.g., surface cation exchange), may ultimately allow optimization of the surface free energies to achieve maximum stabilization of the iodide elpasolite phase relative to its decomposition products.

Finally, to test the role of purely kinetic trapping in the formation and stability of this iodide elpasolite, we prepared Cs<sub>2</sub>AgBiBr<sub>6</sub> polycrystalline thin films (100–200 nm grain sizes, see Figure S17) by thermal evaporation and attempted to convert these to Cs<sub>2</sub>AgBiI<sub>6</sub> by anion exchange, as was done with the NCs. Notably, these grains possess no surface ligands and have much lower surface-to-volume ratios than the colloidal NCs ( $\sim 0.04 \, vs \sim 0.40 \, \text{nm}^{-1}$ ), but ion mobility is sufficient for the entire grain volume to remain accessible (see, e.g., refs 30, 52, and 53 for analogous anion-exchange reactions on lead-halide perovskite films). We previously demonstrated a strong thermodynamic driving force and near-stoichiometric reactivity for TMSX reagents in anion exchange of both perovskites and elpasolites.<sup>9,30</sup> Figure 7 presents absorption and XRD data for a representative anion-exchange experiment on one of these thin films. With a single dose (5 molar equiv) of gas-phase TMSI, the absorption spectrum shows the pronounced low-energy peak decrease in intensity and shift to slightly longer wavelengths,

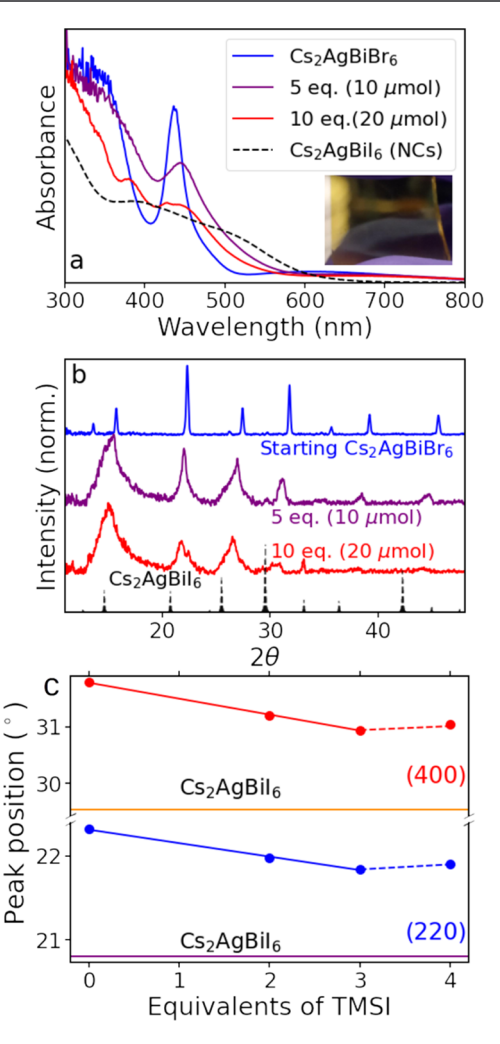


Figure 7. (a) Absorption spectra (inset: photograph of starting thin film) and (b) XRD data collected for a thermally evaporated thin film of  $Cs_2AgBiBr_6$  at various stages of TMSI addition. A stoichiometric excess of TMSI (10  $\mu$ mol, similar to the quantities used in the above nanocrystal reactions) was used in both additions and allowed to react for ~24 h. Analysis of the XRD peak shifts suggests a terminal composition of  $Cs_2AgBi(Br_{0.66}I_{0.34})_6$ . (c) Peak positions as a function of equivalents of TMSI. Further anion exchange was not observed beyond 3 equiv. For reference, the yellow and purple horizontal lines denote the positions of the (400) and (220) peaks in  $Cs_2AgBiI_6$ , respectively.

consistent with partial anion exchange. With a second dose of TMSI, this absorption band simply decreases in intensity and the optical quality of the film was observed by eye to degrade, suggesting decomposition. The XRD data in Figure 7b confirm these observations, showing a shift in the elpasolite peak positions with the first dose of TMSI corresponding to anion alloying and formation of Cs<sub>2</sub>AgBi(Br<sub>0.66</sub>I<sub>0.34</sub>)<sub>6</sub>, but no further movement of the elpasolite peaks is observed upon delivering the second dose of TMSI. Instead, peak broadening is observed, consistent with a decrease in crystallinity. Anion exchange proceeded more slowly in these thin films than in the NCs, and we therefore allowed samples to react for ~24 h to ensure completion after each dose. Additional doses of TMSI or slower dosing with longer reaction times (Figures 7c and S16) both failed to yield any further anion exchange beyond Cs2AgBi- $(Br_{0.66}I_{0.34})_6$ . Using an extremely large dose of TMSI (~100-fold excess) decomposed the sample to yield a mixture of Cs<sub>3</sub>Bi<sub>2</sub>I<sub>9</sub>, AgI, and CsI, with additional minor impurities. Overall these

results indicate that the elpasolite structure is stable only up to  $Cs_2AgBi(Br_{0.66}I_{0.34})_6$  in these films, and further conversion is not possible. This result provides evidence for rejection of the hypothesis that the iodide elpasolite NCs are achieved solely due to kinetic trapping, and it is consistent with the conclusion drawn above that surface free energy (*i.e.*, thermodynamics) plays a critical role in stabilizing the iodide elpasolite phase.

One possible balanced chemical reaction describing Cs<sub>2</sub>AgBiI<sub>6</sub> decomposition is given by eq 1.

$$2Cs_2AgBiI_6 \rightarrow Cs_3Bi_2I_9 + 2AgI + CsI$$
 (1

The free-energy driving force for this reaction at the nanoscale  $(\Delta G_{\text{rxn,NC}})$  involves contributions from the lattice (taken as  $\Delta G_{\rm rxn,bulk}$ ), from the change in ligand binding between reactants and products ( $\Delta G_{\text{ligand}}$ ), and from any change in intrinsic surface free energies between reactants and products ( $\Delta G_{\text{surface}}$ ). The data presented here argue that the magnitude of  $\Delta G_{\text{ligand}}$  +  $\Delta G_{
m surface}$  must exceed that of  $\Delta G_{
m rxn,bulk}$  for at least some of the ligands examined here. A quantitative analysis of these free energies is complicated by the fact that the thermodynamics of ligand binding to Cs<sub>2</sub>AgBiI<sub>6</sub>, Cs<sub>3</sub>Bi<sub>2</sub>I<sub>9</sub>, AgI, and CsI NCs are not documented. Additionally, decomposition does not generally yield the stoichiometric ratio of crystalline products described by eq 1 (e.g., Scheme 1), indicating that additional product species must be accounted for. A full thermodynamic analysis of Cs<sub>2</sub>AgBiI<sub>6</sub> NC decomposition will thus require careful experimentation to quantify these many contributing factors.

## CONCLUSIONS

The data and analysis presented here provide the first definitive structural characterization of any iodide elpasolite. Rietveld refinement of high-energy XRD and PDF data collected from Cs<sub>2</sub>AgBiI<sub>6</sub> nanocrystals shows them to exhibit an elpasolite structure with tetragonal  $(\overline{I4m})$  symmetry. High-energy XRD and PDF measurements show that the elpasolite structure gradually expands during anion exchange to accommodate the larger iodide ions as it evolves continuously from cubic Cs<sub>2</sub>AgBiBr<sub>6</sub> to tetragonal Cs<sub>2</sub>AgBiI<sub>6</sub>. Fitting the PDF data using the refined structure model reveals evidence of surface relaxation, and additional experiments probing the effects of surface ligation and grain size strongly support the conclusion that the elpasolite structure of Cs<sub>2</sub>AgBiI<sub>6</sub> is stabilized by the surface free energy (i.e., thermodynamics) of these nanocrystals. The detailed structural characterization presented here, along with the identification of factors influencing the stability of the elpasolite phase, provides a valuable foundation for future exploration and application of this and yet-undiscovered members of the extremely rare iodide elpasolite family of compounds. These results further emphasize the unique opportunities that exist for developing this family of compounds when working at the nanoscale.

## ASSOCIATED CONTENT

# **Supporting Information**

The Supporting Information is available free of charge at https://pubs.acs.org/doi/10.1021/acs.chemmater.3c01511.

Absorbance of Cs<sub>2</sub>AgBiBr<sub>6</sub> nanocrystals (blue) and anion-exchanged Cs<sub>2</sub>AgBiI<sub>6</sub> nanocrystals (orange) used for X-ray total scattering measurements (Figure S1); X-ray scattering data collected for Cs<sub>2</sub>AgBiI<sub>6</sub> nanocrystals (Figure S2); comparison of Rietveld refinement results using synchrotron X-ray scattering data for Cs<sub>2</sub>AgBiI<sub>6</sub>

nanocrystals (Figure S3); example radial distribution function of the residuals from the Rietveld refinements (Figure S4); residuals after last Rietveld refinement for each structure considered here (Table S1); Rietveld refinement results using synchrotron X-ray scattering data (Figures S5 and S6); synchrotron XRD patterns for each sample in a series from Cs2AgBiBr6 to Cs2AgBiI6 plotted in Q-space (Figure S7); real-space fit to the Cs<sub>2</sub>AgBiI<sub>6</sub> PDF data using cubic  $(Fm\overline{3}m)$  and tetragonal  $(\overline{I4}m)$ structural models, run using pdfgui (Figures S8 and S9); absorption spectra and XRD patterns (Figure S10); TEM images of  $Cs_2AgBiX_6$  (X = Br, I) nanocrystals exposed to various organic compounds (Figure S11); absorption and XRD data for Cs<sub>2</sub>AgBiI<sub>6</sub> nanocrystals (Figure S12); TEM images of the  $Cs_2AgBiX_6$  (X = Br, I) nanocrystals from Figure S12 (Figure S13); absorption and XRD data for Cs<sub>2</sub>AgBiBr<sub>6</sub> nanocrystals exposed to various small molecules (Figure S14); TEM images of Cs<sub>2</sub>AgBiBr<sub>6</sub> nanocrystals exposed to select small-molecule additives (Figure S15); water contents of select additives and solvents measured using Karl-Fischer titration (Table S2); gradual anion exchange of a thermally evaporated thin film of Cs<sub>2</sub>AgBiBr<sub>6</sub> using TMSI vapor (Figure S16); SEM EDX mapping of finalpolycrystalline thin film from slow anion-exchange reaction series (Figure S17); XRD patterns of Cs<sub>2</sub>AgBiI<sub>6</sub> nanocrystal film samples heated to various temperatures under nitrogen atmosphere for 30 min (ex situ) (Figure S18); SEM images of Cs<sub>2</sub>AgBiI<sub>6</sub> nanocrystal thin films before and after heating (ex situ) (Figure S19); in situ XRD data for a film of Cs<sub>2</sub>AgBiI<sub>6</sub> nanocrystals heated in air (Figure S20); TEM images of in situ heating experiments on Cs2AgBiI6 nanocrystals (Figure S21); additional TEM images of in situ heating experiments on Cs<sub>2</sub>AgBiI<sub>6</sub> nanocrystals with deliberately broad size distribution, including large branched nanorods (Figure S22); absorption spectra of Cs<sub>2</sub>AgBiI<sub>6</sub> nanocrystals heated in hexanes solution (Figure S23); and TEM EDX data for a representative  $Cs_2AgBiX_6$  (X = Br, I) elpasolite NC sample prepared from Cs<sub>2</sub>AgBiBr<sub>6</sub> NCs by partial anion exchange using TMSI (Figure S24) (PDF)

# AUTHOR INFORMATION

## **Corresponding Author**

Daniel R. Gamelin — Department of Chemistry, University of Washington, Seattle, Washington 98195, United States;
o orcid.org/0000-0003-2888-9916; Email: gamelin@chem.washington.edu

### Authors

**Kyle T. Kluherz** – Department of Chemistry, University of Washington, Seattle, Washington 98195, United States; orcid.org/0000-0002-7986-5167

Sebastian T. Mergelsberg — Physical Sciences Division, Pacific Northwest National Laboratory, Richland, Washington 99352, United States; oorcid.org/0000-0003-3483-5244

James J. De Yoreo — Physical Sciences Division, Pacific Northwest National Laboratory, Richland, Washington 99352, United States; oorcid.org/0000-0002-9194-6699

Complete contact information is available at: https://pubs.acs.org/10.1021/acs.chemmater.3c01511

#### Notes

The authors declare no competing financial interest.

## ACKNOWLEDGMENTS

This research was primarily supported by the UW Molecular Engineering Materials Center, an NSF Materials Research Science and Engineering Center (grant no. DMR-1719797). Synchrotron X-ray data analysis was supported by the DOE Office of Science, Office of Basic Energy Sciences, Chemical Sciences, Geosciences, and Biosciences Division, Geosciences Program at Pacific Northwest National Laboratory (PNNL) under FWP 56674. PNNL is a multiprogram national laboratory operated for the DOE by Battelle Memorial Institute under Contract DE-AC05-76RL0-1830. Part of this work was conducted at the Molecular Analysis Facility, a National Nanotechnology Coordinated Infrastructure (NNCI) site at the University of Washington, which is supported in part by funds from the National Science Foundation (awards NNCI-2025489 and NNCI-1542101), the Molecular Engineering & Sciences Institute, and the Clean Energy Institute. The authors acknowledge Scott Braswell for his assistance with SEM & EDX measurements. TEM heating data using an in situ heating holder were collected in the William R. Wiley Environmental Molecular Sciences Laboratory (EMSL), a national scientific user facility sponsored by DOE's Office of Biological and Environmental Research and located at Pacific Northwest National Laboratory. The authors thank Libor Kovarik for his assistance with these experiments. This research used resources of the Advanced Photon Source, a U.S. Department of Energy (DOE) Office of Science User Facility operated for the DOE Office of Science by Argonne National Laboratory under Contract No. DE-AC02-06CH11357. The authors thank Leighanne Gallington and Olaf Borkiewicz from Sector 11 (BL 11-ID-B) for assistance collecting data presented in this manuscript.

## ■ REFERENCES

- (1) Pan, Y.; Zhang, Y.; Kang, W.; Deng, N.; Yan, Z.; Sun, W.; Kang, X.; Ni, J. Progress in the preparation and application of CsPbX<sub>3</sub> perovskites. *Mater. Adv.* **2022**, *3*, 4053–4068.
- (2) Ling, X.; Yuan, J.; Ma, W. The Rise of Colloidal Lead Halide Perovskite Quantum Dot Solar Cells. *Acc. Mater. Res.* **2022**, *3*, 866–878.
- (3) Dey, A.; Ye, J.; De, A.; Debroye, E.; Ha, S. K.; Bladt, E.; Kshirsagar, A. S.; Wang, Z.; Yin, J.; Wang, Y.; Quan, L. N.; Yan, F.; Gao, M.; Li, X.; Shamsi, J.; Debnath, T.; Cao, M.; Scheel, M. A.; Kumar, S.; Steele, J. A.; Gerhard, M.; Chouhan, L.; Xu, K.; Wu, X.-g.; Li, Y.; Zhang, Y.; Dutta, A.; Han, C.; Vincon, I.; Rogach, A. L.; Nag, A.; Samanta, A.; Korgel, B. A.; Shih, C.-j.; Gamelin, D. R.; Son, D. H.; Zeng, H.; Zhong, H.; Sun, H.; Demir, H. V.; Scheblykin, I. G.; Mora-Seró, I.; Stolarczyk, J. K.; Zhang, J. Z.; Feldmann, J.; Hofkens, J.; Luther, J. M.; Pérez-Prieto, J.; Li, L.; Manna, L.; Bodnarchuk, M. I.; Kovalenko, M. V.; Roeffaers, M. B. J.; Pradhan, N.; Mohammed, O. F.; Bakr, O. M.; Yang, P.; Müller-Buschbaum, P.; Kamat, P. V.; Bao, Q.; Zhang, Q.; Krahne, R.; Galian, R. E.; Stranks, S. D.; Bals, S.; Biju, V.; Tisdale, W. A.; Yan, Y.; Hoye, R. L. Z.; Polavarapu, L. State of the Art and Prospects for Halide Perovskite Nanocrystals. ACS Nano 2021, 15, 10775–10981.
- (4) Nair, S. S.; Krishnia, L.; Trukhanov, A.; Thakur, P.; Thakur, A. Prospect of double perovskite over conventional perovskite in photovoltaic applications. *Ceram. Int.* **2022**, *48*, 34128–34147.
- (5) Savory, C. N.; Walsh, A.; Scanlon, D. O. Can Pb-Free Halide Double Perovskites Support High-Efficiency Solar Cells? *ACS Energy Lett.* **2016**, *1*, 949–955.
- (6) Bartesaghi, D.; Slavney, A. H.; Gélvez-Rueda, M. C.; Connor, B. A.; Grozema, F. C.; Karunadasa, H. I.; Savenije, T. J. Charge Carrier

- Dynamics in Cs<sub>2</sub>AgBiBr<sub>6</sub> Double Perovskite. J. Phys. Chem. C 2018, 122, 4809–4816.
- (7) Chen, X.; Jia, M.; Xu, W.; Pan, G.; Zhu, J.; Tian, Y.; Wu, D.; Li, X.; Shi, Z. Recent Progress and Challenges of Bismuth-Based Halide Perovskites for Emerging Optoelectronic Applications. *Adv. Opt. Mater.* **2023**, *11*, No. 2202153.
- (8) Ghosh, S.; Shankar, H.; Kar, P. Recent developments of lead-free halide double perovskites: a new superstar in the optoelectronic field. *Mater. Adv.* **2022**, *3*, 3742–3765.
- (9) Creutz, S. E.; Crites, E. N.; De Siena, M. C.; Gamelin, D. R. Colloidal Nanocrystals of Lead-Free Double-Perovskite (Elpasolite) Semiconductors: Synthesis and Anion Exchange To Access New Materials. *Nano Lett.* **2018**, *18*, 1118–1123.
- (10) Sk, M. Recent progress of lead-free halide double perovskites for green energy and other applications. *Appl. Phys. A* **2022**, *128*, No. 462.
- (11) Bello, O. O.; Emetere, M. E. Progress and limitation of lead-free inorganic perovskites for solar cell application. *Sol. Energy* **2022**, *243*, 370–380.
- (12) Vishnoi, P.; Seshadri, R.; Cheetham, A. K. Why are Double Perovskite Iodides so Rare? *J. Phys. Chem. C* **2021**, *125*, 11756–11764.
- (13) Zhang, T.; Cai, Z.; Chen, S. Chemical Trends in the Thermodynamic Stability and Band Gaps of 980 Halide Double Perovskites: A High-Throughput First-Principles Study. *ACS Appl. Mater. Interfaces* **2020**, *12*, 20680–20690.
- (14) Rajeev Kumar, N.; Radhakrishnan, R. Electronic, optical and mechanical properties of lead-free halide double perovskites using first-principles density functional theory. *Mater. Lett.* **2018**, 227, 289–291.
- (15) Tripathi, M. N.; Saha, A.; Singh, S. Structural, elastic, electronic and optical properties of lead-free halide double perovskite  $Cs_2AgBiX_6$  (X = Cl, Br, and I). *Mater. Res. Express* **2019**, *6*, 115517.
- (16) Zarabinia, N.; Rasuli, R. Electronic and optical properties of halide double-perovskites under strain: a density functional study. *Energy Sources, Part A* **2021**, *43*, 2443–2455.
- (17) Anbarasan, R.; Srinivasan, M.; Suriakarthick, R.; Albalawi, H.; Sundar, J. K.; Ramasamy, P.; Mahmood, Q. Exploring the structural, mechanical, electronic, and optical properties of double perovskites of  $Cs_2AgInX_6$  (X = Cl, Br, I) by first-principles calculations. *J. Solid State Chem.* **2022**, *310*, No. 123025.
- (18) Volonakis, G.; Filip, M. R.; Haghighirad, A. A.; Sakai, N.; Wenger, B.; Snaith, H. J.; Giustino, F. Lead-Free Halide Double Perovskites via Heterovalent Substitution of Noble Metals. *J. Phys. Chem. Lett.* **2016**, *7*, 1254–1259.
- (19) Filip, M. R.; Liu, X.; Miglio, A.; Hautier, G.; Giustino, F. Phase Diagrams and Stability of Lead-Free Halide Double Perovskites Cs<sub>2</sub>BB'X<sub>6</sub>: B = Sb and Bi, B' = Cu, Ag, and Au, and X = Cl, Br, and I. *J. Phys. Chem. C* **2018**, 122, 158–170.
- (20) Creutz, S. E.; Liu, H.; Kaiser, M. E.; Li, X.; Gamelin, D. R. Structural Diversity in Cesium Bismuth Halide Nanocrystals. *Chem. Mater.* **2019**, *31*, 4685–4697.
- (21) Sansom, H. C.; Longo, G.; Wright, A. D.; Buizza, L. R. V.; Mahesh, S.; Wenger, B.; Zanella, M.; Abdi-Jalebi, M.; Pitcher, M. J.; Dyer, M. S.; Manning, T. D.; Friend, R. H.; Herz, L. M.; Snaith, H. J.; Claridge, J. B.; Rosseinsky, M. J. Highly Absorbing Lead-Free Semiconductor Cu<sub>2</sub>AgBiI<sub>6</sub> for Photovoltaic Applications from the Quaternary CuI—AgI—BiI<sub>3</sub> Phase Space. *J. Am. Chem. Soc.* **2021**, *143*, 3983—3992.
- (22) Glodo, J.; van Loef, E. V. D.; Higgins, W. M.; Shah, K. S. Scintillation Properties of Cs<sub>2</sub>NaLaI<sub>6</sub>:Ce; IEEE, 2006; pp 1208–1211.
- (23) Gundiah, G.; Brennan, K.; Yan, Z.; Samulon, E. C.; Wu, G.; Bizarri, G. A.; Derenzo, S. E.; Bourret-Courchesne, E. D. Structure and scintillation properties of Ce<sup>3+</sup>-activated Cs<sub>2</sub>NaLaCl<sub>6</sub>, Cs<sub>3</sub>LaCl<sub>6</sub>, Cs<sub>2</sub>NaLaBr<sub>6</sub>, Cs<sub>3</sub>LaBr<sub>6</sub>, Cs<sub>2</sub>NaLaI<sub>6</sub> and Cs<sub>3</sub>LaI<sub>6</sub>. *J. Lumin.* **2014**, 149, 374–384.
- (24) Zhang, C.; Gao, L.; Teo, S.; Guo, Z.; Xu, Z.; Zhao, S.; Ma, T. Design of a novel and highly stable lead-free  $Cs_2NaBiI_6$  double perovskite for photovoltaic application. Sustainable Energy Fuels **2018**, 2, 2419–2428.

- (25) Zheng, Y.; Luo, F.; Ruan, L.; Tong, J.; Yan, L.; Sun, C.; Zhang, X. A facile fabrication of lead-free Cs<sub>2</sub>NaBiI<sub>6</sub> double perovskite films for memory device application. *J. Alloys Compd.* **2022**, *909*, No. 164613.
- (26) Bhorde, A.; Waykar, R.; Rondiya, S. R.; Nair, S.; Lonkar, G.; Funde, A.; Dzade, N. Y.; Jadkar, S. Structural, Electronic, and Optical Properties of Lead-Free Halide Double Perovskite Rb<sub>2</sub>AgBil<sub>6</sub>: A Combined Experimental and DFT Study. *ES Mater. Manuf.* **2021**, *12*, 43–52.
- (27) Shadabroo, M. S.; Abdizadeh, H.; Golobostanfard, M. R. Elpasolite structures based on A<sub>2</sub>AgBiX<sub>6</sub> (A: MA, Cs, X: I, Br): Application in double perovskite solar cells. *Mater. Sci. Semicond. Process.* **2021**, *125*, No. 105639.
- (28) Yang, B.; Chen, J.; Yang, S.; Hong, F.; Sun, L.; Han, P.; Pullerits, T.; Deng, W.; Han, K. Lead-Free Silver-Bismuth Halide Double Perovskite Nanocrystals. *Angew. Chem., Int. Ed.* **2018**, *57*, 5359–5363. (29) Pai, N.; Chatti, M.; Fürer, S. O.; Scully, A. D.; Raga, S. R.; Rai, N.; Tan, B.; Chesman, A. S. R.; Xu, Z.; Rietwyk, K. J.; Reddy, S. S.; Hora, Y.; Sepalage, G. A.; Glück, N.; Lira-Cantú, M.; Bach, U.; Simonov, A. N. Solution Processable Direct Bandgap Copper-Silver-Bismuth Iodide Photovoltaics: Compositional Control of Dimensionality and Optoelectronic Properties. *Adv. Energy Mater.* **2022**, *12*, No. 2201482.
- (30) Creutz, S. E.; Crites, E. N.; De Siena, M. C.; Gamelin, D. R. Anion Exchange in Cesium Lead Halide Perovskite Nanocrystals and Thin Films Using Trimethylsilyl Halide Reagents. *Chem. Mater.* **2018**, *30*, 4887–4891.
- (31) Kroupa, D. M.; Crane, M. J.; Gamelin, D. R. Single-Source Flash Sublimation of Metal-Halide Semiconductors; SPIE, 2019; Vol. 11084, 110840I-7.
- (32) Hoeher, A.; Mergelsberg, S.; Borkiewicz, O. J.; Dove, P. M.; Michel, F. M. A new method for in situ structural investigations of nanosized amorphous and crystalline materials using mixed-flow reactors. *Acta Crystallogr., Sect. A: Found. Adv.* **2019**, *75*, 758–765.
- (33) Toby, B. H.; Von Dreele, R. B. GSAS-II: the genesis of a modern open-source all purpose crystallography software package. *J. Appl. Crystallogr.* **2013**, *46*, 544–549.
- (34) Juhás, P.; Davis, T.; Farrow, C. L.; Billinge, S. J. L. PDFgetX3: a rapid and highly automatable program for processing powder diffraction data into total scattering pair distribution functions. *J. Appl. Crystallogr.* **2013**, *46*, 560–566.
- (35) Farrow, C. L.; Juhas, P.; Liu, J. W.; Bryndin, D.; Božin, E. S.; Bloch, J.; Proffen, T.; Billinge, S. J. L. PDFfit2 and PDFgui: computer programs for studying nanostructure in crystals. *J. Phys.: Condens. Matter* **2007**, *19*, 335219.
- (36) Filip, M. R.; Hillman, S.; Haghighirad, A. A.; Snaith, H. J.; Giustino, F. Band Gaps of the Lead-Free Halide Double Perovskites Cs<sub>2</sub>BiAgCl<sub>6</sub> and Cs<sub>2</sub>BiAgBr<sub>6</sub> from Theory and Experiment. *J. Phys. Chem. Lett.* **2016**, *7*, 2579–2585.
- (37) Billinge, S. J. L.; Kanatzidis, M. G. Beyond crystallography: the study of disorder, nanocrystallinity and crystallographically challenged materials with pair distribution functions. *Chem. Commun.* **2004**, 749–760.
- (38) Egami, T.; Billinge, S. J. L. Underneath the Bragg Peaks: Structural Analysis of Complex Materials, 2nd ed.; Pergamon, 2012.
- (39) Billinge, S. J. L.; Levin, I. The problem with determining atomic structure at the nanoscale. *Science* **2007**, *316*, 561–565.
- (40) Li, M.; Zhang, X.; Lu, S.; Yang, P. Phase transformation, morphology control, and luminescence evolution of cesium lead halide nanocrystals in the anion exchange process. *RSC Adv.* **2016**, *6*, 103382–103389.
- (41) Nedelcu, G.; Protesescu, L.; Yakunin, S.; Bodnarchuk, M. I.; Grotevent, M. J.; Kovalenko, M. V. Fast Anion-Exchange in Highly Luminescent Nanocrystals of Cesium Lead Halide Perovskites (CsPbX<sub>3</sub>, X = Cl, Br, I). *Nano Lett.* **2015**, *15*, 5635–5640.
- (42) Fu, Y.; Wu, T.; Wang, J.; Zhai, J.; Shearer, M. J.; Zhao, Y.; Hamers, R. J.; Kan, E.; Deng, K.; Zhu, X. Y.; Jin, S. Stabilization of the Metastable Lead Iodide Perovskite Phase via Surface Functionalization. *Nano Lett.* **2017**, *17*, 4405–4414.

- (43) Tappan, B. A.; Brutchey, R. L. Polymorphic Metastability in Colloidal Semiconductor Nanocrystals. *ChemNanoMat* **2020**, *6*, 1567–1588
- (44) Soni, U.; Arora, V.; Sapra, S. Wurtzite or zinc blende? Surface decides the crystal structure of nanocrystals. *CrystEngComm* **2013**, *15*, 5458–5463.
- (45) Mahler, B.; Lequeux, N.; Dubertret, B. Ligand-Controlled Polytypism of Thick-Shell CdSe/CdS Nanocrystals. *J. Am. Chem. Soc.* **2010**, *132*, 953–959.
- (46) Bekenstein, Y.; Dahl, J. C.; Huang, J.; Osowiecki, W. T.; Swabeck, J. K.; Chan, E. M.; Yang, P.; Alivisatos, A. P. The Making and Breaking of Lead-Free Double Perovskite Nanocrystals of Cesium Silver–Bismuth Halide Compositions. *Nano Lett.* **2018**, *18*, 3502–3508.
- (47) Dahl, J. C.; Osowiecki, W. T.; Cai, Y.; Swabeck, J. K.; Bekenstein, Y.; Asta, M.; Chan, E. M.; Alivisatos, A. P. Probing the Stability and Band Gaps of Cs<sub>2</sub>AgInCl<sub>6</sub> and Cs<sub>2</sub>AgSbCl<sub>6</sub> Lead-Free Double Perovskite Nanocrystals. *Chem. Mater.* **2019**, *31*, 3134–3143.
- (48) Krieg, F.; Ochsenbein, S. T.; Yakunin, S.; ten Brinck, S.; Aellen, P.; Süess, A.; Clerc, B.; Guggisberg, D.; Nazarenko, O.; Shynkarenko, Y.; Kumar, S.; Shih, C.-J. J.; Infante, I.; Kovalenko, M. V. Colloidal  $CsPbX_3$  (X = Cl, Br, I) Nanocrystals 2.0: Zwitterionic Capping Ligands for Improved Durability and Stability. *ACS Energy Lett.* **2018**, 3, 641–646
- (49) Stelmakh, A.; Aebli, M.; Baumketner, A.; Kovalenko, M. V. On the Mechanism of Alkylammonium Ligands Binding to the Surface of CsPbBr<sub>3</sub> Nanocrystals. *Chem. Mater.* **2021**, *33*, 5962–5973.
- (50) Veldhuis, S. A.; Tay, Y. K. E.; Bruno, A.; Dintakurti, S. S. H.; Bhaumik, S.; Muduli, S. K.; Li, M.; Mathews, N.; Sum, T. C.; Mhaisalkar, S. G. Benzyl Alcohol-Treated CH<sub>3</sub>NH<sub>3</sub>PbBr<sub>3</sub> Nanocrystals Exhibiting High Luminescence, Stability, and Ultralow Amplified Spontaneous Emission Thresholds. *Nano Lett.* **2017**, *17*, 7424–7432.
- (51) Sun, J.-K.; Huang, S.; Liu, X.-Z.; Xu, Q.; Zhang, Q.-H.; Jiang, W.-J.; Xue, D.-J.; Xu, J.-C.; Ma, J.-Y.; Ding, J.; Ge, Q.-Q.; Gu, L.; Fang, X.-H.; Zhong, H.-Z.; Hu, J.-S.; Wan, L.-J. Polar Solvent Induced Lattice Distortion of Cubic CsPbI<sub>3</sub> Nanocubes and Hierarchical Self-Assembly into Orthorhombic Single-Crystalline Nanowires. *J. Am. Chem. Soc.* **2018**, *140*, 11705–11715.
- (52) Li, G.; Ho, J. Y.-L.; Wong, M.; Kwok, H. S. Reversible Anion Exchange Reaction in Solid Halide Perovskites and Its Implication in Photovoltaics. *J. Phys. Chem. C* **2015**, *119*, 26883–26888.
- (53) Hoffman, J. B.; Schleper, A. L.; Kamat, P. V. Transformation of Sintered CsPbBr<sub>3</sub> Nanocrystals to Cubic CsPbI<sub>3</sub> and Gradient CsPbBr<sub>x</sub>I<sub>3-x</sub> through Halide Exchange. *J. Am. Chem. Soc.* **2016**, *138*, 8603–8611.